Hindawi
International Journal of Energy Research
Volume 2024, Article ID 6648691, 15 pages
https://doi.org/10.1155/2024/6648691

WILEY | Hindawi

Research Article

Model Predictive Control on Transient Flux Linkage and Reactive Power Compensation of Doubly Fed Induction Wind Generator

Jian-hong Zhu,[1] **Pengkun Zhang**,[1] **Xinsong Zhang**,[1] **Lin Qin**,[1] **Chengxiang Sun**,[2] **and Han Li**[1]

[1]*School of Electrical Engineering and Automation, Nantong University, Nantong, China*
[2]*School of Electrical and Automation, Lianyungang Normal College, Lianyungang, China*

Correspondence should be addressed to Jian-hong Zhu; jh.zhu@ntu.edu.cn

Received 9 November 2023; Revised 7 January 2024; Accepted 29 January 2024; Published 5 March 2024

Academic Editor: Yogendra Arya

For weak grid scenario with high new energy proportion, large fluctuations of load are prone to cause low-voltage ride through. Moreover, stator transient magnetic flux will cause overvoltage and overcurrent problems in the rotor of doubly fed induction generator. Based on model predictive control, a control strategy for transient flux linkage and reactive power compensation is proposed. Firstly, regarding the issue of reactive power allocation of grid side converters (GSC) and rotor side converters (RSC), an allocation strategy is derived under minimizing winding energy loss on case of low-voltage ride through, enabling the wind energy conversion system to provide reactive power support during grid voltage recovery process. Meanwhile, an improved mixed second- and third-order generalized integrator (MSTOGI) phase-locked loop (PLL) is used to extract the positive and negative sequence components of the power grid voltage, further for RSC control. Secondly, in response to power grid faults, considering the influence of stator DC transient flux and negative sequence flux components on rotor current, by injecting rotor transient compensation current and stator flux feedforward compensation into RSC, the rotor impulse voltage and loop current are reduced. Moreover, combined with model predictive control algorithm, a control strategy of rotor current is designed. Finally, a simulation platform is built to validate the effectiveness of the proposed method based on comparing with several traditional vector control low-voltage ride through methods.

1. Introduction

The rapid development of the global economy has exacerbated the speed of traditional fossil fuel depletion and environmental degradation. It is urgent to continuously develop the new energy technologies [1, 2]. Now, the proportion of wind power in the total grid power generation is increasing rapidly and has exceeded 733 GW [3]. Among which, the wind energy conversion system (WECS) based on doubly fed induction generators (DFIG) has been widely used due to high wind energy capture efficiency [4], mature wind power generation control technology, and small converter capacity [5, 6].

However, due to the special linking structure that stator winding connects to the power grid directly, DFIG is very sensitive to grid disturbances [7]. Once a power grid fault occurs, a large induced EMF (electromotive force) in the rotor circuit will be generated for the reason that stator flux cannot change suddenly with the stator voltage, so resulting in transient overvoltage and overcurrent of the rotor [8]. Especially under asymmetric faults in the power grid, negative sequence voltage components in the stator would exacerbate the oscillation of rotor side overvoltage and overcurrent [9].

Heretofore, disturbances and faults in the power grid would greatly affect the reliable operation and self-protection of DFIG, a typical example is the ability to ride through low voltage (LVRT). The LVRT technologies involved in existing literature are mainly divided into two categories, hardware intervention and software control [10]. Hardware protection technology depends on the speed of material science development, so the breakthrough speed is relatively slow. In software

technology, the literature research results mainly present the control of back-to-back converters, and typical demagnetization methods are using the stator flux as a feedforward compensation for the RSC, effectively improving the LVRT capability of DFIG [11, 12]. By adding demagnetization current to RSC, the stator DC and negative sequence flux components of the stator can be reduced, and the LVRT capability of DFIG can be enhanced [13]. Hence, wavelet packet transform has been used for transient stability analysis of DC bus voltage [14]. In reference [15], Kumar and Chatterjee used the artificial bee colony algorithm to solve the maximum power point tracking problem by considering rotor speed as an optimization problem to improve system robustness. In addition, the combination use of supercapacitor energy storage components and passive series dynamic resistors can effectively control rotor overcurrent and overvoltage and suppress fluctuations in DC bus voltage [16]. A virtual capacitor control strategy is introduced to reduce the impact of line impedance by compensating for the output angle deviation of the PLL and improves the stability of DFIG [17].

In terms of hardware protection measures, crowbar protection and chopping protection are commonly used in the LVRT process of DFIG [18]. Followed by which, collaborative control of two types of protection is utilized to cope with electromagnetic changes in DFIG [19]. A two-level three-phase converter is proposed, which compensates for stator voltage drop by connecting the converter in series with the power grid [20]. In addition, in the event of a low-voltage fault in the power grid, a fault current limiter based on a new type of iron core material reduces the peak fault current by increasing the line impedance [21].

Of course, the reliability of grid-connected power generation control must take into account the entire process of fault occurrence, troubleshooting, and system recovery. As a key technology of PLL, it is necessary to accurately extract the fundamental power grid voltage parameters accurately. In reference [22], Vijay et al. used a hybrid generalized integral filter to filter out the DC bias voltage and harmonics contained in the power grid voltage. Followed by which, a new control strategy for symmetric PLL was proposed [23]. A virtual impedance design scheme was designed to improve the output current frequency stability of DFIG. Moreover, considering the shortcomings of the widely used proportional integral (PI) control in DFIG control systems [24, 25], a model predictive control (MPC) scheme is proposed in RSC control design [26], which can predict future behavior based on the system model. Due to understandable and good dynamic performance, MPC has been widely used [27], where the switch state of the rotor side converter is taken as the control input and augmented decision variables are introduced, thereby reducing computational control time and improving DFIG control performance [28]. The research did not pay more attention to the scenario of grid harmonics and LVRT.

Due to the uncertainty of weather conditions and the complexity of the model of DFIG, to prevent the disconnection problem of DFIG system in weak grid operation, as well consider strong robustness and good control performance of MPC under uncertainty process, innovative exploration of control methods is performed under multigrid fault scenarios based on previous research results. During the period of voltage drop in the power grid, the DFIG rotor side induces a large peak current, which in turn damages the inverter equipment. Therefore, this article first studies the impact of stator transient magnetic flux caused by voltage drop in the power grid on rotor current. A collaborative control is proposed by reactive power compensation and MPC for stator transient flux, to minimize the amplitude of rotor current and voltage during power grid faults.

Highlights of the work are the following: (1) By introducing a stator flux feedforward compensation strategy, the transient speeds of flux attenuation of the stator and the system recovery are all accelerated. (2) By injecting reverse rotor current to control the injection of rotor current and rotor terminal voltage angle, all are suppressed. (3) Considering the problem of inaccurate voltage phase detection in traditional PLL during power grid voltage faults, an improved MSTOGI-PLL is proposed to accurately lock the grid voltage and improve the stability of the wind power generation system. (4) Considering winding losses in DFIG, a reactive power allocation strategy of stator and rotor is proposed to reduce the total winding losses, which provides reactive power support for grid voltage recovery certainly, as well as control strategy to protect the safe and stable operation of DFIG.

The remainder of this paper is organized as follows: Section 2 describes the grid-connected power generation model for wind energy conversion systems. The electromagnetic transient analysis process of DFIG under LVRT is presented in Section 3. Section 4 provides LVRT control strategy based on MPC. Section 5 discusses the simulation results of the system in different cases. Finally, Section 6 concludes the study.

2. Grid-Connected Power Generation Model for WECS

Figure 1 shows that WECS includes modules such as a DFIG, energy storage battery, transformer, power grid, and load. The energy storage battery is connected to the DC bus capacitor through a DC/DC converter. Wind turbine is controlled in maximum power tracking mode. The MPC control models of the GSC and RSC are also shown in the figure. The goal is to reduce the total winding loss of the DFIG and provide reactive power support for grid restoration.

In the case of voltage drop, rotor overvoltage and overcurrent are reduced by injecting reverse rotor current. At the same time, by increasing stator flux feedforward compensation, the transient magnetic flux attenuation speed is accelerated, so rotor overcurrent is suppressed. Furthermore, to accurately detect the phase and frequency of nonideal grid voltage, an improved MSTOGI-PLL structure is proposed. Based on which, reactive power allocation strategies are adopted on the rotor side and grid side under the consideration of winding losses of DFIG, as well as the need for which to absorb reactive power during the voltage recovery process of the grid. The wind power system model and control strategy are analyzed as follows. By comparing with

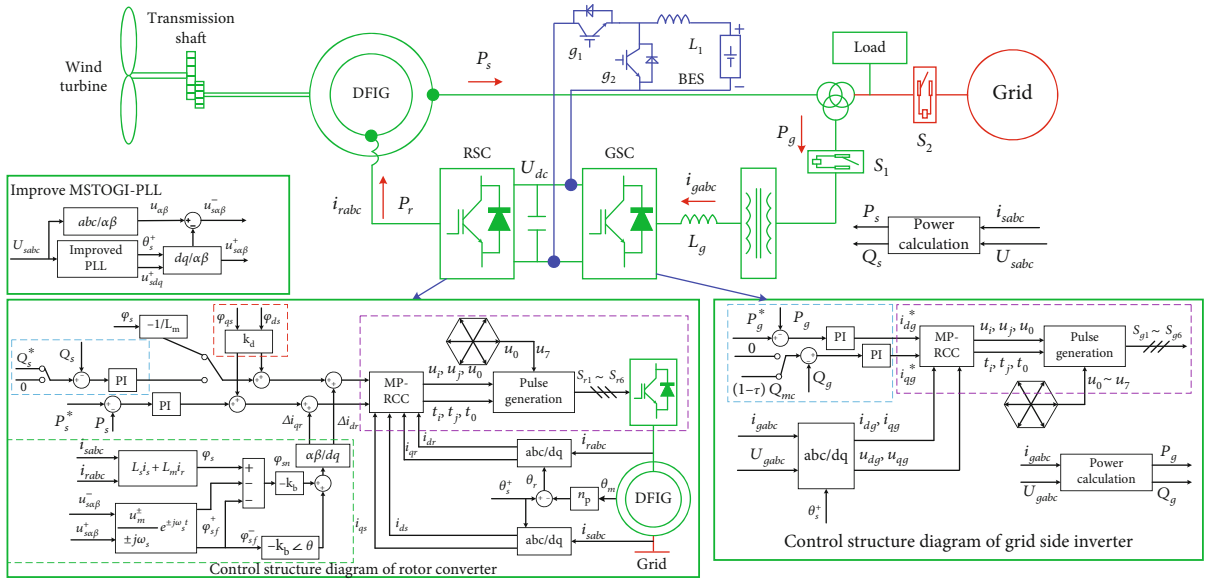

Figure 1: Detailed model structure diagram of doubly fed wind motor.

traditional control strategies, the simulation results verify the superiority of the proposed control strategy, significantly enhancing the fault traversal ability of DFIG.

2.1. Wind Energy Capture Model. In the design of simulation parameters, consider the acceleration gear mechanism. A 5 kW wind turbine is designed at a rated wind speed of 10 m/s. The captured power of the wind turbine is P_m [29].

$$P_m = 0.5 \times \rho \pi r^2 v^3 C_p(\lambda, \beta), \tag{1}$$

where ρ is the air density, r is the turbine radius, v is the current wind speed, $C_p(\lambda, \beta)$ is the wind energy utilization coefficient, λ is the tip speed ratio, and β is the yaw angle. Relationship of $C_p(\lambda, \beta)$ and λ can be expressed as follows:

$$\begin{cases} C_p(\lambda, \beta) = 0.517\left(\dfrac{116}{\lambda_i} - 0.45\beta - 5\right)e^{-21/\lambda_i} + 0.0068\lambda, \\ \dfrac{1}{\lambda_i} = \dfrac{1}{\lambda + 0.08\beta} - \dfrac{0.035}{\beta^3 + 1}, \\ \lambda = \dfrac{r\omega_t}{v} = \dfrac{r\omega_r}{\eta v}, \end{cases} \tag{2}$$

where $\beta = 0$, ω_t is the fan blade angular velocity, η is the gearbox ratio, and ω_r is the DFIG rotor speed. For the used experimental prototype parameters of DFIG simulation platform, refer to literature [30]. $s(-30\% \sim 30\%)$, $u_{rms} = 380$ V, $f_s = 50$ Hz, $R_s = 1.32\,\Omega$, $R_r = 1.708\,\Omega$, $n_p = 2$, $L_m = 219$ mH, $L_{lr} = 6.832$ mH, $L_{ls} = 6.832$ mH, and $U_{dc} = 240$ V. Transformer ratio is as follows: 115 : 380; $\omega_s = 314$ rad/s.

2.2. Calculation of Stator and Rotor Losses and Reactive Power Distribution. In order to reduce the losses of DFIG stator and rotor windings, as well as reduce the peak current on the rotor side under grid faults, and provide reactive power support for grid voltage recovery, it is necessary to analyze the RSC and GSC reactive power distribution coefficients of DFIG excitation to improve the LVRT capability of WECS.

The reactive power required for DFIG magnetization calculation is as follows:

$$Q_{mc} = \frac{v_l^2}{2\pi f_s L_m} = \frac{380^2}{2 \times \pi \times 50 \times 0.219} = 2.1\,\text{kvar}, \tag{3}$$

where Q_{mc} is the DFIG magnetization reactive power, f_s is the grid frequency, v_l is the line voltage of the power grid, and L_m is the mutual inductance between the stator and rotor.

Here, the DFIG excitation power provided by GSC is assumed as $Q_s = (1-\tau)Q_{mc}$, $\tau(0 < \tau < 1)$, which is the reactive power distribution coefficient. The provided reactive power of RSC is $Q_r = \tau s Q_{mc}$. When the wind power generation system operates stably, the calculation for stator and rotor winding losses W_{all} is as follows:

$$\begin{aligned} W_{\text{all}} &= W_s + W_r = 3I_s^2 R_s + 3I_r^2 R_r = 3\left(\frac{S_s}{\sqrt{3}v_l}\right)^2 R_s + 3\left(\frac{S_r}{\sqrt{3}|s|v_l}\right)^2 R_r \\ &= \frac{1}{v_l^2}\left((P_s^2 + Q_s^2)R_s + \frac{P_r^2 + Q_r^2}{s^2}R_r\right) \\ &= \frac{1}{v_l^2}\left((P_s^2 + (1-\tau)^2 Q_{mc}^2)R_s + \frac{s^2 P_s^2 + \tau^2 s^2 Q_{mc}^2}{s^2}R_r\right) \\ &= \frac{1}{v_l^2}\left(\left(P_s^2(R_s + R_r) + Q_{mc}^2\left((R_s + R_r)\tau^2 - 2R_s\tau + R_s\right)\right.\right). \end{aligned} \tag{4}$$

In Eq. (4), W_s and W_r are the stator and rotor winding losses, I_s and I_r are stator and rotor current, and S_s and S_r are stator and rotor windings capacity.

To realize W_{all} minimum, namely, to find the minimum value of a quadratic function $(R_s + R_r)\tau^2 - 2R_s\tau + R_s$ with respect to τ, the peak value is obtained when $\tau = R_s/(R_s + R_r)$. Substituting which into Eq. (4) yields

$$W_{\text{all\_min}} = W_s + W_r = \frac{1}{v_l^2}\left(P_s^2(R_s + R_r) + Q_{mc}^2\left(\frac{-R_s^2}{R_s + R_r} + R_s\right)\right). \tag{5}$$

When the excitation power is fully provided by RSC, $\tau = 1$. At this point, the rotor winding loss W_{all} is as follows:

$$W_{\text{all}} = W_s + W_r = \frac{1}{v_l^2}\left(P_s^2(R_s + R_r) + Q_{mc}^2 R_r\right). \tag{6}$$

Subtracting Eq. (5) from Eq. (6) yields

$$\begin{aligned}\Delta W_{\text{all}} = W_{\text{all}} - W_{\text{all\_min}} &= \frac{1}{v_l^2}\left(Q_{mc}^2\left(R_r - \left(\frac{-R_s^2}{R_s + R_r} + R_s\right)\right)\right) \\ &= \frac{1}{v_l^2} Q_{mc}^2 \frac{R_r^2}{R_s + R_r}.\end{aligned} \tag{7}$$

According to Eq. (7), $\Delta W_{\text{all}} > 0$; therefore, the total copper loss of DFIG winding can be reduced.

2.3. Grid-Connected PLL Model. Figure 2 shows the improved MSTOGI-PLL structure, which is used to decompose the positive and negative sequence components of the power grid voltage. A feedforward compensation link is added to the traditional MSTOGI structure to enhance the attenuation speed of the amplitude of the low-frequency and high-frequency harmonic components contained in the three-phase voltage.

Figure 2(a) shows the improved MSTOGI structure diagram. Among them, $D_1(s)$ and $Q_1(s)$ have the same amplitude frequency characteristics. The transfer function is as follows:

$$\begin{cases} D_1(s) = \dfrac{u_1(s)}{u(s)} = \dfrac{k\omega_0\omega_1 s}{s^3 + \omega_1 s^2 + (k\omega_0\omega_1 + \omega_0^2)s + \omega_0^2\omega_1}, \\ Q_1(s) = \dfrac{u_2(s)}{u(s)} = \dfrac{k\omega_0\omega_1 s}{s^3 + \omega_1 s^2 + (k\omega_0\omega_1 + \omega_0^2)s + \omega_0^2\omega_1} \times \dfrac{(-s + \omega_0)}{(s + \omega_0)}, \end{cases} \tag{8}$$

where s is a Laplace transform operator (s not the slip rate), $u_1(s)$ and $u_2(s)$ are two mutually orthogonal output signals, $u_1(s)$ leads 90 degrees ahead of the phase $u_2(s)$, $u_3(s)$ represents the DC voltage component contained in the three-phase voltage, $u(s)$ is the input voltage signal, k is the damping coefficient, ω_0 is the resonant frequency, and ω_1 is the frequency of the compensation phase.

Figure 2(b) shows a nonlinear PI regulator model; construction is as follows:

$$k_p[e(t)] = \begin{cases} k_p - a_1 k_p[1 - \text{sech}\ (a_3 e(t))] & e(t) > |e(t)|_{\max}, \\ k_p - a_2 k_p[1 - \text{sech}\ (a_3 e(t))] & e(t) \le |e(t)|_{\max}, \end{cases} \tag{9}$$

where sech $(x) = 2/(e^x + e^{-x})$ is a hyperbolic secant function, k_p is the value of the conventional PI regulator, a_1 is the value when it exceeds the frequency deviation threshold, a_2 is the value when $e(t)$ is within the frequency deviation threshold range, sech $(a_3 e(t))$ is a hyperbolic function, and a_3 is the attenuation coefficient of which. According to Eq. (9), when the output frequency of the PLL is consistent with the three-phase voltage frequency, $k_p[e(t)] = k_p$. According to the polarity of the deviation, namely, $e(t)$ is a positive or negative deviation, determine whether the value exceeds the deviation threshold, further to select an appropriate curve value $k_p[e(t)]$ that varies with the error. Construction is as follows:

$$k_i[e(t)] = k_i\ \text{sech}\ (ce(t)), \tag{10}$$

where k_i is the value of the conventional PI regulator and c is the attenuation coefficient of the hyperbolic function. In Eq. (10), when $e(t) = 0$, $k_i[e(t)] = k_i$. When $e(t)$ increases, $k_i[e(t)]$ gradually decreases to prevent oscillation in the response and reduce overshoot. The specific parameter selection in the paper is shown in Table 1.

The results of single-phase voltage drop and two-phase voltage drop are shown in Figure 3, including improved mixed second- and third-order generalized integrator PLL (MSTOGI2 in the figure), delay signal cancellation PLL (DSC in the figure), double second-order generalized integrator PLL (DSOGI in the figure), and traditional mixed second- and third-order generalized integrator PLL (MSTOGI1 in the figure). It can be seen from which that the proposed MSTOGI2 PLL can more accurately extract the frequency and phase of grid voltage when a fault happens.

3. Electromagnetic Transient Analysis and Control

3.1. Stator Flux Feedforward Compensation. Assuming that both the stator and rotor adopt the motor convention, and the rotor side parameters are converted to the stator side, the grid voltage experienced a symmetrical fault drop with a depth of d at time t_0. Ignoring the stator resistance R_s, the stator flux can be represented as the steady-state flux and transient DC flux components due to that the stator flux cannot change suddenly before and after the grid voltage drop. The differential equation can be expressed as follows [31].

$$\varphi_s = \varphi_{sf} + \varphi_{sn} = \frac{(1 - d)u_m}{j\omega_s} e^{j\omega_s t} + \frac{du_m}{j\omega_s} e^{-t/\tau_s} e^{-t/\tau_s}, \tag{11}$$

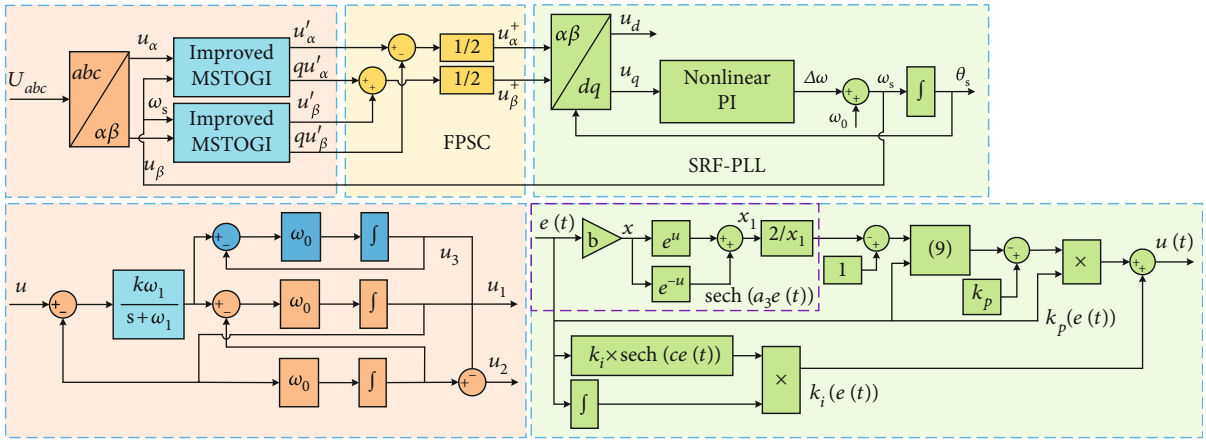

(a) Improved MSTOGI (b) Nonlinear PI

Figure 2: (a) Improved MSTOGI-PLL and (b) nonlinear PI structure.

Table 1: Variable speed wind turbine system parameters.

Controller parameters	GSC power outer ring: $k_{p1} = 0.001$, $k_{i1} = 1.5$ RSC power outer ring: $k_{p2} = 0.002$, $k_{i2} = 0.001$
MSTOGI-PLL parameter	$k = 1.414$, $\omega_1 = 628$, $a_1 = 0.04$, $a_2 = 0.08$, $a_3 = 2$, $c = 1.5$

where $\tau_s = L_s/R_s$ is the stator time constant. According to Eq. (11), only when the transient DC flux φ_{sn} gradually decays to zero can the system enter a new stable state.

In the case of asymmetric grid voltage faults, according to the symmetrical component method and superposition principle, the stator voltage space vector is represented as follows:

$$u_s = u_m^+ e^{j\omega_s t} + u_m^- e^{-j\omega_s t} + u_{m0}. \tag{12}$$

In Eq. (12), u_m^+, u_m^-, and u_{m0} are the amplitude of the positive sequence, negative sequence, and zero sequence voltage components, respectively. Once asymmetric grid voltage drop occurs, originating from positive sequence voltage and negative sequence voltage, the steady-state magnetic flux component of the stator is generated.

So, during asymmetric faults, the stator magnetic flux φ_s is as follows [32].

$$\varphi_s = \frac{u_m^+}{j\omega_s} e^{j\omega_s t} + \frac{u_m^-}{-j\omega_s} e^{-j\omega_s t} + \frac{u_m + u_m^- - u_m^+}{j\omega_s} e^{-t/\tau_s}, \tag{13}$$

where φ_{sf}^+ and φ_{sf}^- are the steady-state magnetic flux generated by the positive and negative sequence voltages of the stator.

According to Eq. (13), including the positive sequence and transient flux components, the influence of negative sequence flux is also necessary to be considered in the case of asymmetric faults.

According to the DFIG state space model, the stator flux state equation in the dq synchronous rotating coordinate system is as follows [33].

$$\begin{cases} p\varphi_{ds} = u_{ds} - \dfrac{R_s}{L_s}\varphi_{ds} + \omega_s\varphi_{qs} + \dfrac{R_s L_m}{L_s} i_{dr}, \\ p\varphi_{qs} = u_{qs} - \dfrac{R_s}{L_s}\varphi_{qs} + \omega_s\varphi_{ds} + \dfrac{R_s L_m}{L_s} i_{qr}. \end{cases} \tag{14}$$

In Eq. (14), u_{ds} and u_{qs} are the stator voltage, φ_{ds} and φ_{qs} are the stator flux, and i_{dr} and i_{qr} are the rotor current.

Solving the system state equations in Eq. (14), characteristic roots of which are $\lambda_s = -R_s/L_s \pm j\omega_s$. Due to small R_s, the transient DC flux decay rate of the stator is very slow. To restore stable operation as soon as possible, a feedforward stator flux fluctuation compensation term is introduced in the rotor current loop. The improved stator flux state equation is as following.

$$\begin{cases} p\varphi_{ds} = u_{ds} - \dfrac{R_s}{L_s}\varphi_{ds} + \omega_s\varphi_{qs} + \dfrac{R_s L_m}{L_s}\left[i_{dr} - k_d(\varphi_{ds} - \varphi_{ds0})\right], \\ p\varphi_{qs} = u_{qs} - \dfrac{R_s}{L_s}\varphi_{qs} + \omega_s\varphi_{ds} + \dfrac{R_s L_m}{L_s}\left[i_{qr} - k_d\left(\varphi_{qs} - \varphi_{qs0}\right)\right], \end{cases} \tag{15}$$

where k_d is the coefficient of stator flux compensation term, $\varphi_{ds0} = 0$ is the steady-state initial value of the stator flux d-axis, and $\varphi_{qs0} = u_m/\omega_s$ is the steady-state initial value of the stator flux q-axis. Solve the system state equations

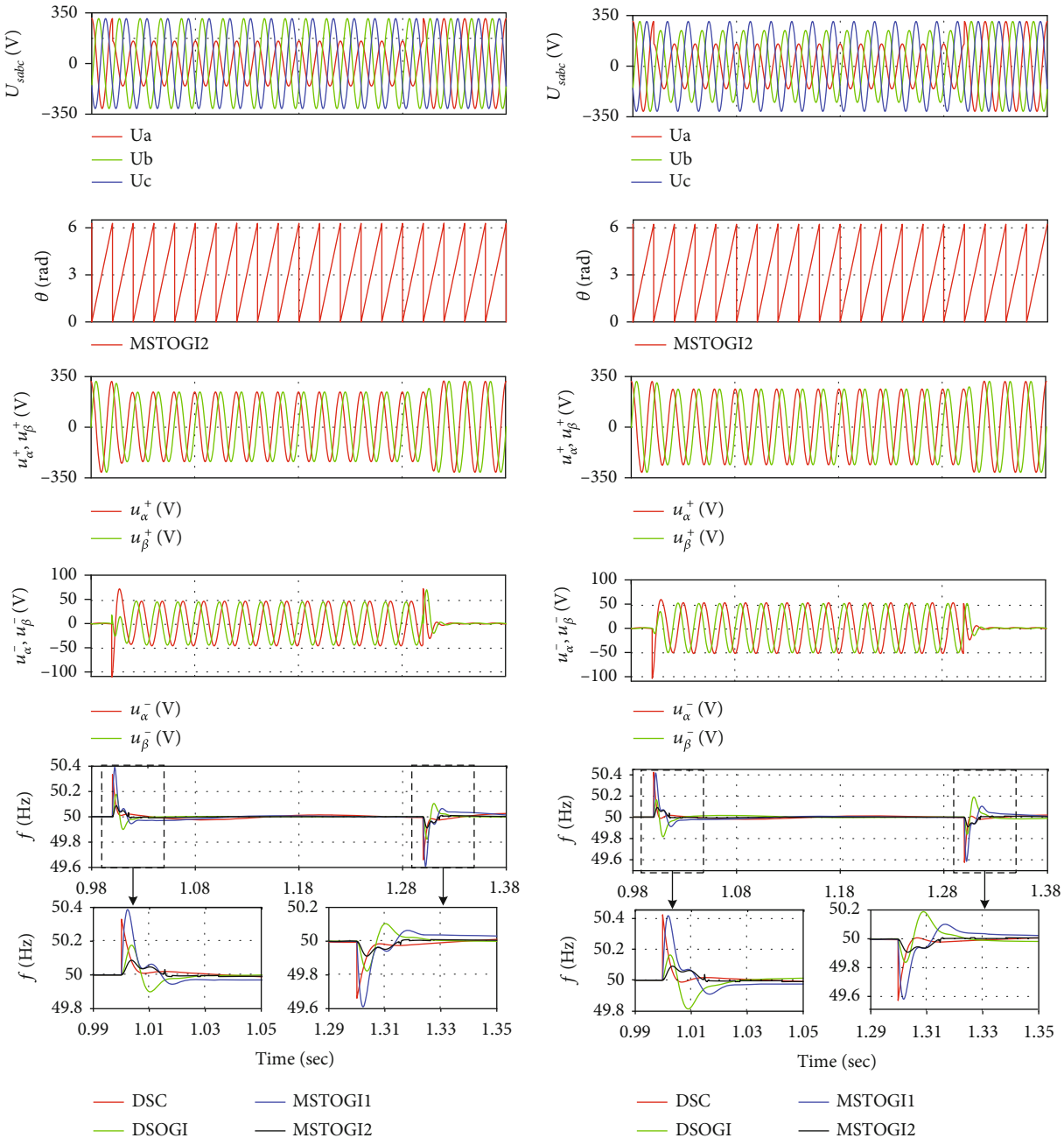

Figure 3: Results of PLL during single-phase and two-phase voltage drop.

in Eq. (15), whose characteristic roots are $\lambda_s = -(R_s/L_s + k_d(L_m/\tau_s)) \pm j\omega_s$. With negative real part of the characteristic root increases, the transient DC flux decay of the stator speed accelerates.

3.2. Transient Compensation of Rotor Current. Considering the capacity limitation of RSC, the induced EMF of the rotor is prone to exceed the controllable voltage range, which will weaken the current limiting ability of RSC and cause overcurrent on the rotor side. Therefore, it is necessary to analyze the rotor side voltage.

When operating in a stable state, the rotor voltage equation u_r is as follows:

$$u_r = k_s(p - j\omega_r)\varphi_s + [R_r + \sigma L_r(p - j\omega_r)]i_r. \quad (16)$$

According to Eq. (11), in the case of grid symmetrical faults, the stator flux includes steady-state flux φ_{sf} and transient DC flux φ_{sn}. Corresponding voltage components are induced at the rotor end, namely, u_{rf} and u_{rn}. Considering

only the transient process of the stator flux linkage, the rotor open circuit voltage u_{rk} is obtained by $i_r = 0$, as follows:

$$u_{rk} = u_{rf} + u_{rn}. \tag{17}$$

Substitute the steady-state flux φ_{sf} and transient DC flux φ_{sn} in Eq. (11) into the first term of Eq. (16), ignoring the smaller term $1/\tau_s$; Eq. (18) is obtained.

$$\begin{cases} u_{rf} = k_s s(1-d)u_m e^{j\omega_s t}, \\ u_{rn} = -k_s\left(\dfrac{1}{\tau_s} + j\omega_r\right)\dfrac{du_m}{j\omega_s}e^{-t/\tau_s} = -k_s(1-s)du_m e^{-t/\tau_s}. \end{cases} \tag{18}$$

In Eq. (18), $s = (\omega_s - \omega_r)/\omega_s$ is the slip rate. In general, the DFIG slip s is within 0.3, so the steady-state induced electromotive force u_{rf} of the rotor is relatively small. However, the transient DC flux-induced EMF u_{rn} of the rotor is proportional to $k_s(1-s)du_m$, and its amplitude is several times higher than that under steady-state conditions. Therefore, there is an excessive peak current in the rotor circuit, which is not conducive to the stability of DFIG.

Multiply Eq. (18) by $e^{-j\omega_r t}$ and convert it to the rotor coordinate system to obtain the following equation:

$$\begin{cases} u^r_{rf} = k_s s(1-d)u_m e^{j(\omega_s-\omega_r)t} = k_s s j\omega_s \varphi^r_{sf}, \\ u^r_{rn} = -k_s(1-s)du_m e^{-t/\tau_s - j\omega_r t} = -k_s(1-s)j\omega_s \varphi^r_{sn}. \end{cases} \tag{19}$$

The superscript r in the equation represents the parameters under the rotor shaft system. The voltage equation in the rotor coordinate system can be expressed as follows:

$$u^r_r = u^r_{rk} + R_r i^r_r + \sigma L_r p i^r_r. \tag{20}$$

When the voltage drops deeply, u^r_{rf} is relatively small. Substitute u^r_{rn} and the transient DC flux current i^r_{rn} into Eq. (20), and convert which to time domain to obtain the transient DC flux-induced voltage component of the rotor as follows:

$$\begin{aligned} u^r_{rn} &= -k_s(1-s)j\omega_s \varphi^r_{sn} + R_r i^r_{rn} - \sigma j\omega_r L_r i^r_{rn} \\ &= -j\omega_r(k_s \varphi^r_{sn} + \sigma L_r i^r_{rn}) + R_r i^r_{rn}. \end{aligned} \tag{21}$$

According to Eq. (21), in order to avoid transient surge voltage at the rotor end, the voltage can be suppressed by accelerating the decay rate of the stator transient DC flux component φ^r_{sn}, injecting rotor current i^r_{rn} opposite to the stator transient DC flux, and increasing rotor impedance.

Ignoring the rotor resistance, $u^r_{rn} = 0$, (22) can be obtained.

$$i^r_{rn} = -\frac{k_s}{\sigma L_r}\varphi^r_{sn}. \tag{22}$$

When the rotor current is not zero and φ^r_{sf} is eliminated, the differential equation of φ^r_{sn} is obtained as follows:

$$p\varphi^r_{sn} = -\frac{1}{\tau_s}\varphi^r_{sn} + \frac{L_m}{L_s}R_s i^r_{rn}. \tag{23}$$

Substitute Eq. (22) into Eq. (23), and the transient DC flux φ^r_{sn} is solved by differential equation, resulting as follows:

$$\varphi^r_{sn} = c^r_{sn0}e^{-t/\tau}, \tag{24}$$

where c^r_{sn0} is the initial value of the transient DC flux φ^r_{sn}, and $\tau_1 = \tau_s/(1 + L_m k_s/(\sigma L_r))$ is the new stator time constant. According to Eq. (24), compensating current on the rotor side can accelerate the stator flux decay rate.

Under asymmetric faults, the rotor terminal voltage can be expressed as follows [34].

$$\begin{aligned} u^r_r = {} & k_s u^+_m s e^{j(\omega_s-\omega_r)t} + k_s u^+_m(2-s)e^{-j(2-s)\omega_s t} - k_s(1-s)j\omega_s \varphi^r_{sn} \\ & + R_r i^r_r + \sigma L_r p i^r_r. \end{aligned} \tag{25}$$

According to Eq. (25), due to that rotor side overvoltage under asymmetric faults caused by stator transient attenuation DC component and negative sequence flux component, the rotor terminal voltage induced by the negative sequence component of the magnetic flux and corresponding transient current can be analyzed based on similar principles as the transient DC component of the magnetic flux.

4. LVRT Control Strategy Based on MPC

4.1. LVRT Prediction Model Based on MPC for Rotor Side. Compared to conventional PI control methods, MPC is a prior control method, with good ability to predict the future behavior and select control variables. The mathematical model of DFIG in stator voltage-oriented synchronous rotating coordinate system is as follows [35].

$$\begin{cases} u_{ds} = R_s i_{ds} + p\varphi_{ds} - \omega_s \varphi_{qs}, \\ u_{qs} = R_s i_{qs} + p\varphi_{qs} + \omega_s \varphi_{ds}, \\ u_{dr} = R_r i_{dr} + p\varphi_{dr} - (\omega_s - \omega_r)\varphi_{qr}, \\ u_{qr} = R_r i_{qr} + p\varphi_{qr} + (\omega_s - \omega_r)\varphi_{dr}, \end{cases} \tag{26}$$

$$\begin{cases} \varphi_{ds} = L_s i_{ds} + L_m i_{dr}, \\ \varphi_{qs} = L_s i_{qs} + L_m i_{qr}, \\ \varphi_{dr} = L_r i_{dr} + L_m i_{ds}, \\ \varphi_{qr} = L_r i_{qr} + L_m i_{qs}, \end{cases} \tag{27}$$

where u_{ds}, u_{qs}, u_{dr}, and u_{qr} are the dq axis components of the stator and rotor voltage; i_{ds}, i_{qs}, i_{dr}, and i_{qr} are the dq axis components of the stator and rotor current; and φ_{ds}, φ_{qs}, φ_{dr}, and φ_{qr} are the dq axis components of the stator and rotor flux linkage.

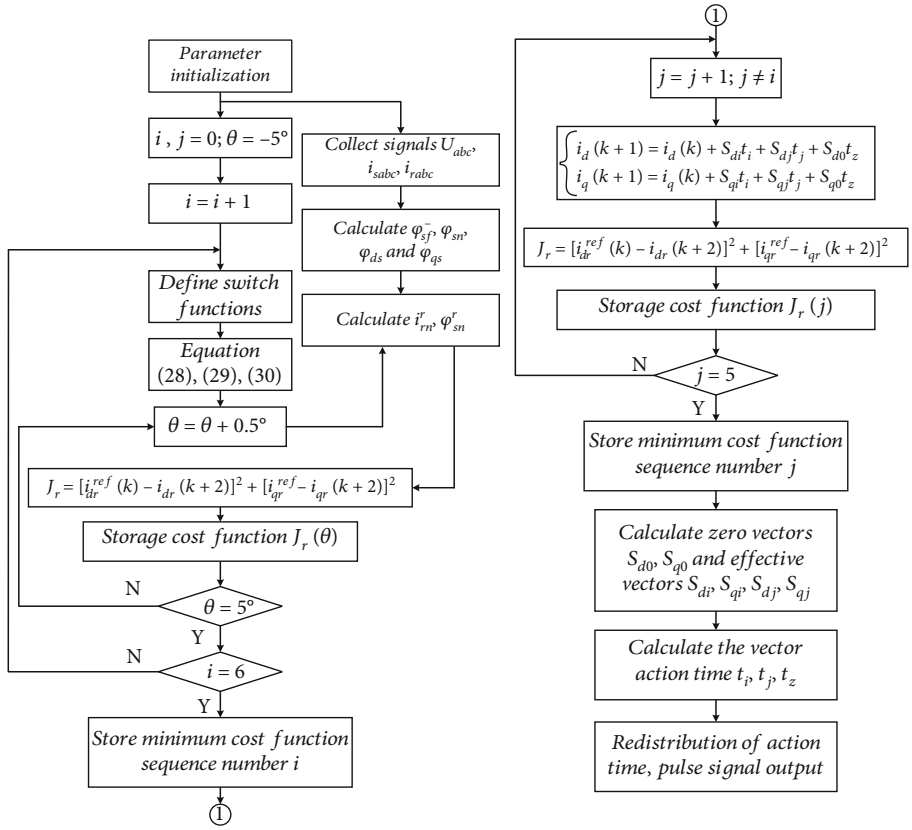

Figure 4: DFIG three-vector MPC calculation flowchart.

Substitute the flux equation in Eq. (27) into the voltage equation in Eq. (26), and perform dq decomposition on the DFIG rotor current, and the rotor current equation is organized as follows.

$$\begin{cases} pi_{dr} = \dfrac{1}{\sigma L_r}\left[-R_r i_{dr} + \left((\omega_s - \omega_r)L_r - \dfrac{\omega_s L_m^2}{L_s}\right) i_{qr} + (R_s L_m / L_s) i_{ds} - \omega_r L_m i_{qs} + u_{dr} - (L_m / L_s) u_{ds}\right], \\ pi_{qr} = \dfrac{1}{\sigma L_r}\left[\left((\omega_r - \omega_s)L_r + \dfrac{\omega_s L_m^2}{L_s}\right) i_{dr} - R_r i_{qr} + \omega_r L_m i_{ds} + (R_s L_m / L_s) i_{qs} + u_{qr} - (L_m / L_s) u_{qs}\right]. \end{cases} \tag{28}$$

Using the forward Euler method, Eq. (28) is done discretize, where $x^{\cdot} = [x(k+1) - x(x)]/T_s$ is the discrete period. Predict the rotor current at time $k+1$, and take into account that the DFIG discretization model has a long delay of one cycle from the step; therefore, $u_{dr}(k)$ and $u_{qr}(k)$ in the rotor current equation are changed to $u_{dr}(k-1)$ and $u_{qr}(k-1)$, and multistep prediction is used to obtain the optimal control quantity through the model prediction algorithm. The prediction equation for rotor current at time $k+1$ is as follows:

$$\begin{cases} i_{dr}(k+1) = i_{dr}(k) + \dfrac{T_s}{\sigma L_r}\left[-R_r i_{dr}(k) + \left((\omega_s - \omega_r)L_r - \dfrac{\omega_s L_m^2}{L_s}\right) i_{qr}(k) + (R_s L_m / L_s) i_{ds}(k) - \omega_r L_m i_{qs}(k) + u_{dr}(k-1) - (L_m / L_s) u_{ds}(k-1)\right], \\ i_{qr}(k+1) = i_{qr}(k) + \dfrac{T_s}{\sigma L_r}\left[\left((\omega_r - \omega_s)L_r + \dfrac{\omega_s L_m^2}{L_s}\right) i_{dr}(k) - R_r i_{qr}(k) + \omega_r L_m i_{ds}(k) + (R_s L_m / L_s) i_{qs}(k) + u_{qr}(k-1) - (L_m / L_s) u_{qs}(k-1)\right]. \end{cases} \tag{29}$$

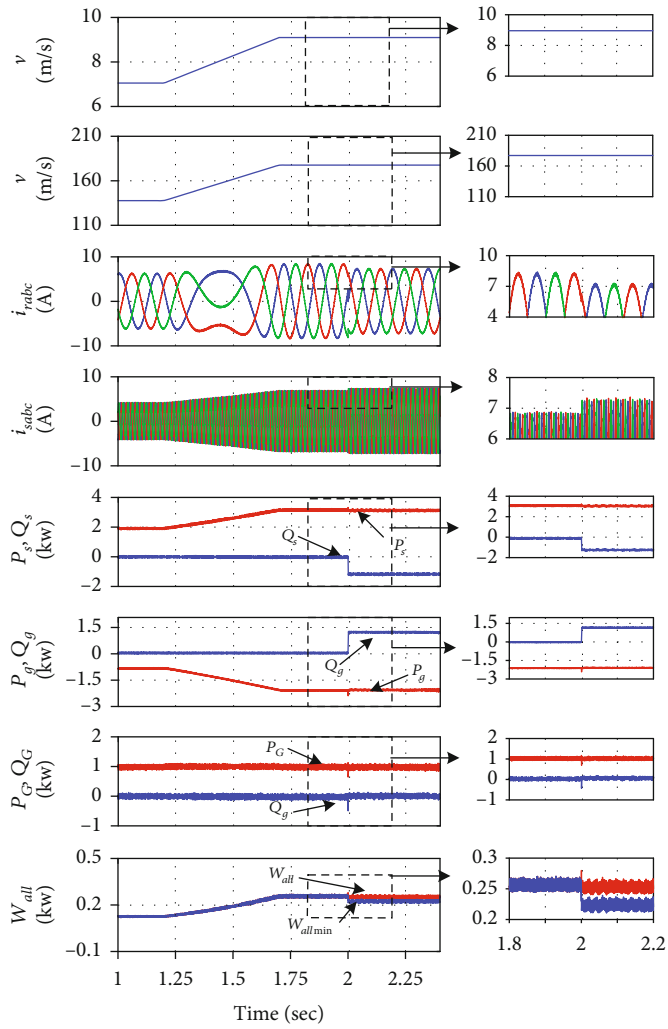

Figure 5: DFIG waveform under different wind speeds.

Table 2: Analysis of DFIG winding losses at a wind speed of 9 m/s.

	I_{ls}	I_{lr}	W_s	W_r
$\tau = 1$	4.877 A	5.828 A	94.19 W	174 W
$\tau = R_s / R_s + R_r$	5.198 A	5.070 A	107 W	131 W
Difference	-0.321 A	0.758 A	-12.8 W	43 W

According to the model predictive control system rolling optimization, eliminating PWM update delay requires a second step prediction of the rotor current. The prediction equation for the rotor current at time k and time $k+2$ is as follows:

$$\begin{cases} i_{dr}(k+2) = i_{dr}(k+1) + \dfrac{T_s}{\sigma L_r}\left[-R_r i_{dr}(k+1) + \left((\omega_s - \omega_r)L_r - \dfrac{\omega_s L_m^2}{L_s}\right) i_{qr}(k+1) + (R_s L_m / L_s) i_{ds}(k+1) - \omega_r L_m i_{qs}(k+1) + u_{dr}(k) - (L_m / L_s) u_{ds}(k)\right], \\ i_{qr}(k+2) = i_{qr}(k+1) + \dfrac{T_s}{\sigma L_r}\left[\left((\omega_r - \omega_s)L_r + \dfrac{\omega_s L_m^2}{L_s}\right) i_{dr}(k+1) - R_r i_{qr}(k+1) + \omega_r L_m i_{ds}(k+1) + (R_s L_m / L_s) i_{qs}(k+1) + u_{qr}(k) - (L_m / L_s) u_{qs}(k)\right]. \end{cases} \tag{30}$$

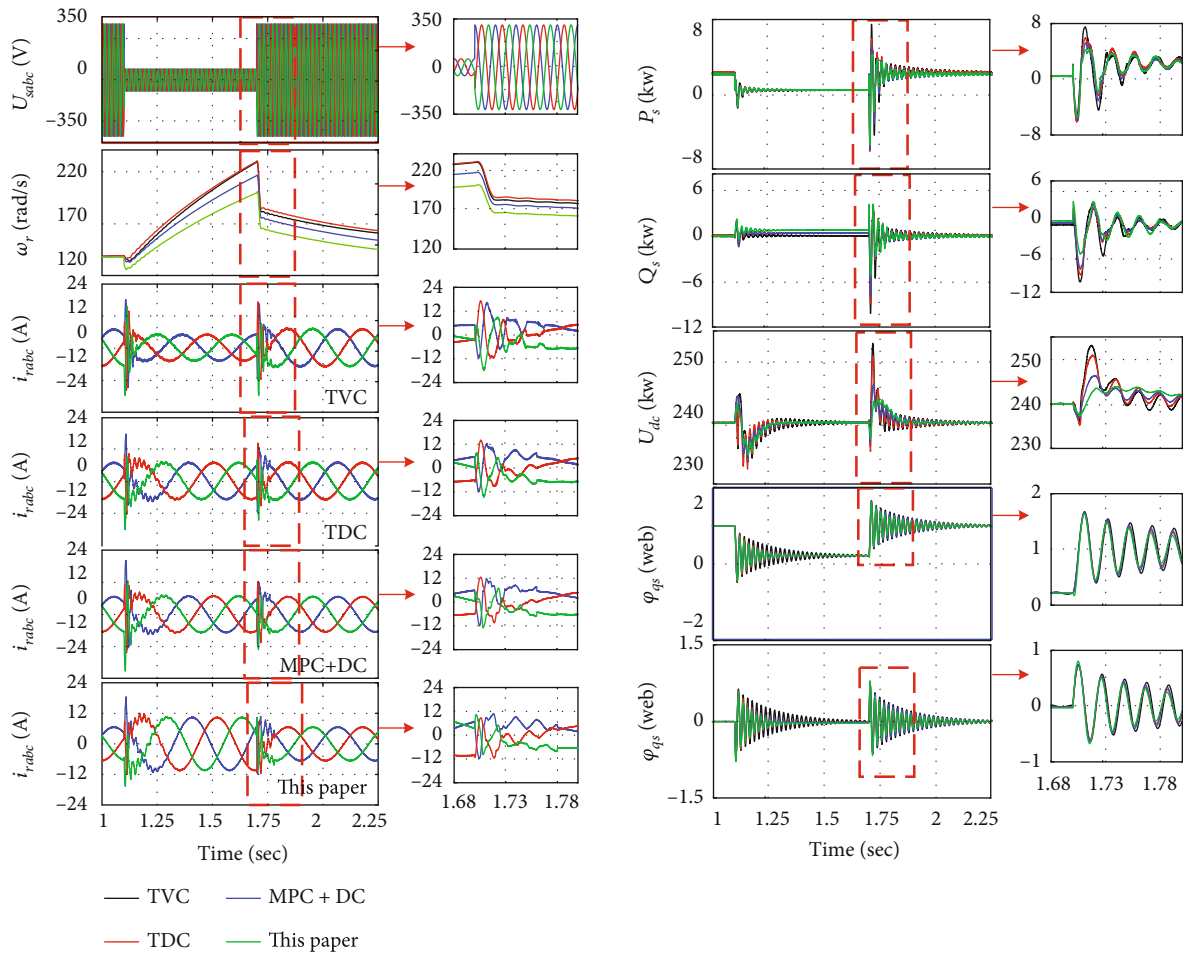

Figure 6: System waveform diagram of three-phase power grid voltage drop.

When DFIG is connected to the grid, the control objective of the rotor current loop is to follow the reference value to the cost function, as follows:

$$J_r = \left[i_{dr}^{\text{ref}}(k) - i_{dr}(k+2)\right]^2 + \left[i_{qr}^{\text{ref}} - i_{qr}(k+2)\right]^2, \quad (31)$$

where J_r is the cost function of rotor current.

4.2. Structure Diagram of System Control Strategy. Figure 4 shows the flowchart of the DFIG three-vector MPC algorithm. Firstly, set parameters such as wind speed, stator, and rotor windings of the doubly fed generator, self-inductance, and mutual inductance. Then, collect the three-phase voltage and current of the power grid for calculating the transient magnetic flux φ_{sn}, negative sequence magnetic flux φ_{sf}^{-}, and magnetic flux φ_{ds} and φ_{qs} of the doubly fed generator stator in the dq rotating synchronous coordinate system. Secondly, calculate the rotor compensation current i_{rn}^{r} and the stator flux feedforward compensation amount φ_{sn}^{r} in the event of a power grid fault. Design a three-vector MPC control algorithm.

Equations (28)–(30) are a discrete mathematical model of a doubly fed generator in the dq coordinate system. Consider the relationship between transient DC flux and transient DC flux compensation current angle θ, so that $\theta = \pm 5°$ changes ($\theta = 0°$ in traditional control schemes) to seek the optimal rotor terminal voltage. The objective function of the rotor side converter is shown in Eq. (31). Substitute i_{dr}^{ref}, i_{qr}^{ref}, $i_{dr}(k+2)$, and $i_{qr}(k+2)$ into the objective function, calculate the first effective vector u_i, and store the switch function number i of the vector. Then, obtain the second effective vector u_j from the remaining 5 switch functions and store the switch function number j of the vector. Finally, calculate the effective action time t_i, t_j, and t_z of the three vectors, and use the seven-segment zero vector distribution SVPWM implementation method to generate pulse output signals to control the DFIG operation.

5. Simulation Case Analysis

To verify the accuracy of the proposed control method, a WECS simulation platform is built on the MATLAB/Simulink system. The reactive power distribution strategy is adopted on the grid side and rotor side to reduce the copper loss of DFIG windings. Secondly, study the changes in rotor circuit current, stator transient magnetic flux, and DC bus voltage under three different operating conditions of symmetrical and asymmetric voltage faults in the power grid.

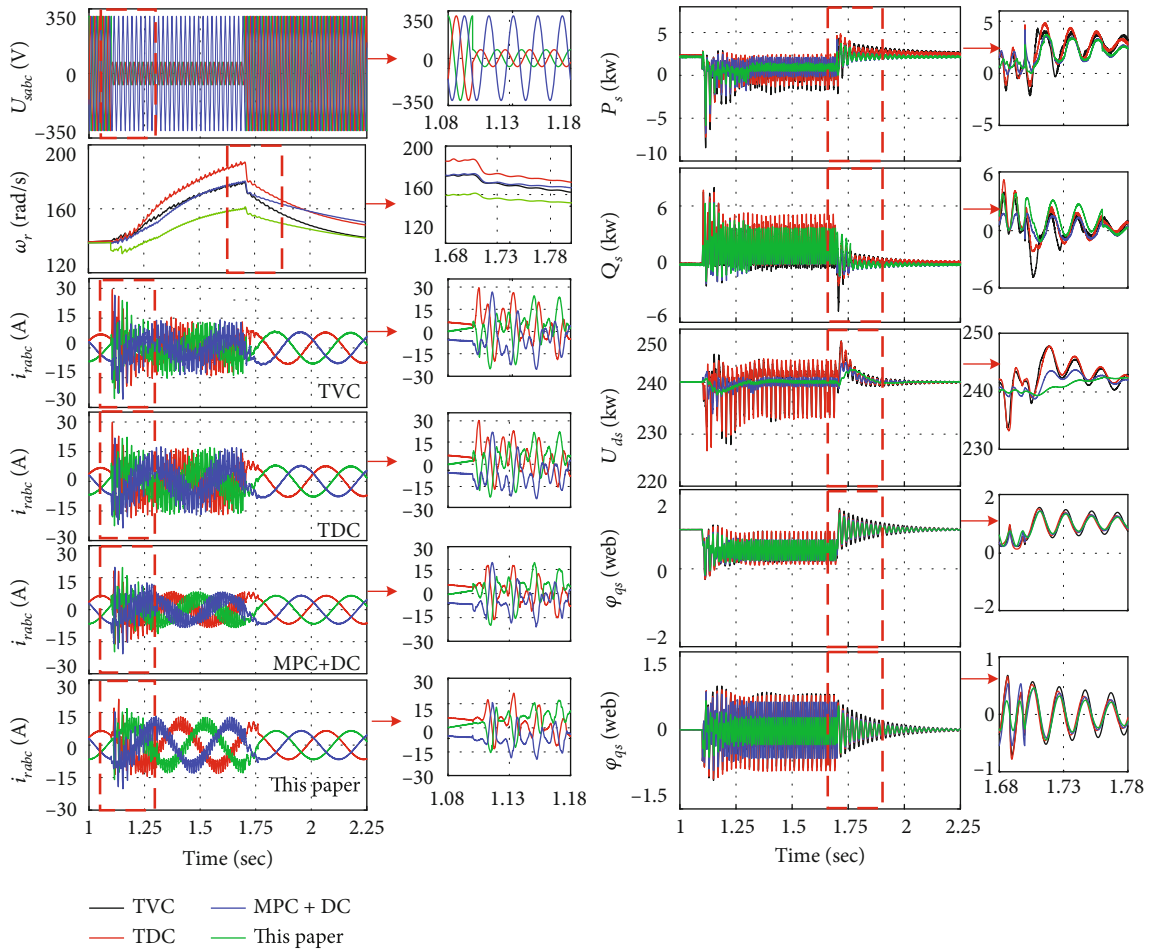

Figure 7: System waveform diagram of two-phase power grid voltage drop.

Further verify that the control strategy can improve the LVRT performance of wind power generation systems.

5.1. Reactive Power Distribution of WECS under Variable Wind Speed. Figure 5 shows the power curve of the wind power generation system as the wind speed changes. The wind speed increased from 7 m/s to 9 m/s. The rotor firstly absorbs power from the grid and then outputs power. The excess energy output by DFIG is absorbed by the battery. At $t = 2$ s, reactive power allocation strategies are executed at the GSC and RSC sides. From the partially enlarged image in Figure 5, it can be seen that as the rotor current increases, and the stator current decreases, while the total winding loss of DFIG decreases, which prove the effectiveness of the control strategy. Table 2 provides an analysis of stator and rotor winding losses at a wind speed of 9 m/s, and the total winding losses are reduced.

5.2. WECS Case Analysis under Grid Fault. To verify the effectiveness of the control strategy proposed, comparisons for waveforms of rotor current and stator flux are done among traditional vector control (TVC), traditional demagnetization control (TDC), MPC+demagnetization control (MPC+DC), and the proposed control strategy. Three scenarios are simulated as following.

Scenario A: analysis of LVRT performance when the three-phase grid voltage drops symmetrically to 20%

Scenario B: analysis of LVRT performance when the two-phase grid voltage drops to 20%

Scenario C: analysis of LVRT performance when the single-phase grid voltage drops to 20%

Figure 6 shows a symmetrical drop in three-phase voltage between $t = 1.1$ s and 1.7 s under scenario A. It can be seen that the rotor speed gradually increases during the drop period, and a maximum rotor current of 2.6 pu occurs by the TVC method, while a rotor current of 1.9 pu occurs by the control strategy proposed, and reactive power support is provided during the voltage recovery period. Compared with traditional vector control strategies, the reactive power absorbed is reduced by 49%, and the minimum fluctuation rate of DC bus voltage is controlled under 2.0%.

Figure 7 shows operating results under scenario B. In the early stage of voltages drop, the rotor speed rapidly increases, and the TVC scheme increases the rotor speed by 37.5%, not conducive to the stability of wind turbines. Among the four control strategies, under the TVC and TDC schemes, the peak rotor current is numerically similar. Applying MPC control technology to DFIG control strategies can reduce the overshoot of DC bus voltage. The rotor current of 2.2 pu occurs by control strategy proposed.

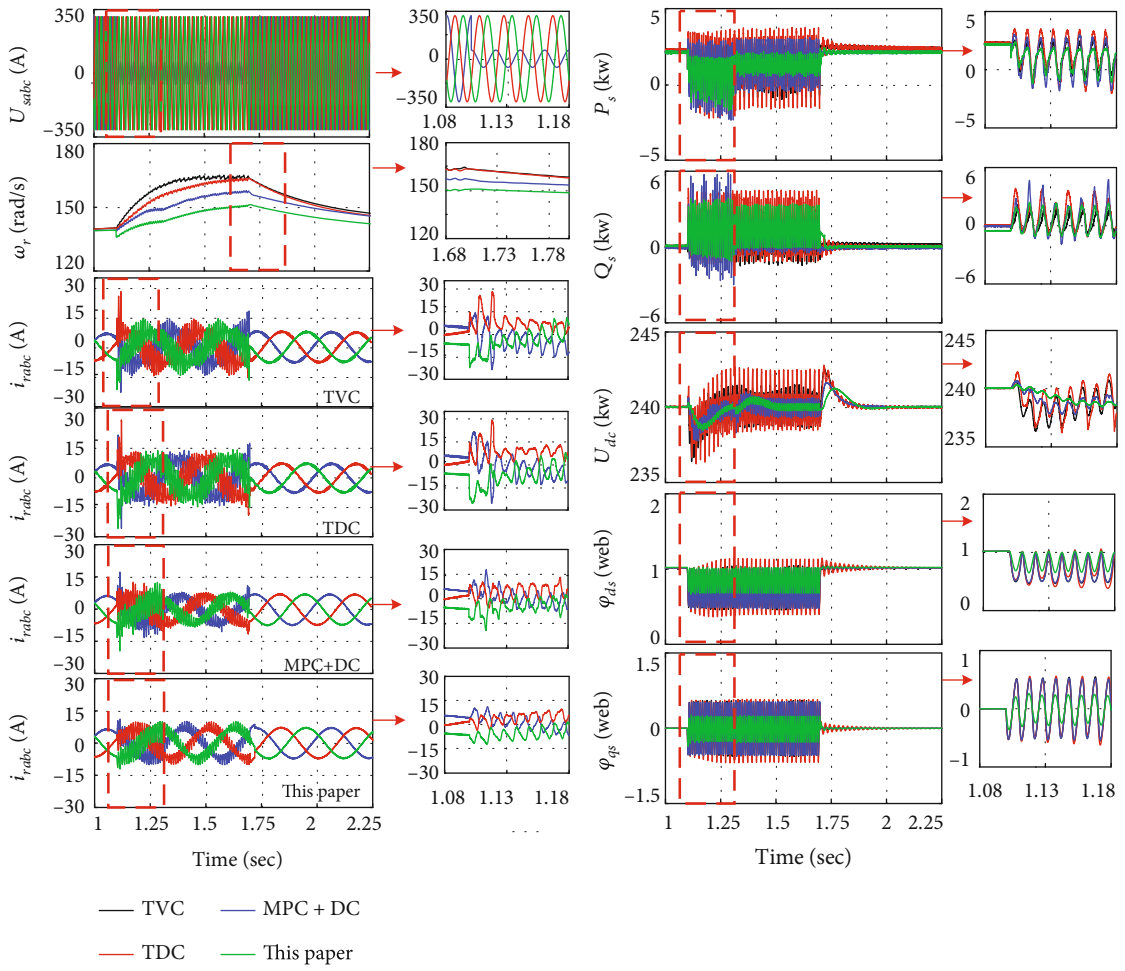

Figure 8: System waveform diagram of single-phase power grid voltage drop.

Table 3: Comparison of relevant control performance indicators.

Index		Peak rotor current (pu)	DC bus voltage overshoot (%)	Stator active power recovery time (s)	Maximum reactive power absorbed by stator (kW)	Rotor speed overshoot (%)
Three-phase voltage drops to 20%	TVC	2.6	5.4	0.7	10.2	64.2
	TDC	2.5	4.5	0.6	9.1	64.2
	MPC+DC	2.5	2.7	0.6	7.8	50.3
	Method proposed	1.9	2.0	0.45	5.2	28.5
Two-phase voltage drop to 20%	TVC	4.1	5.0	1.3	4.9	35.7
	TDC	3.7	5.0	0.9	2.2	25.2
	MPC+DC	2.8	2.5	0.7	1.8	25.0
	Method proposed	2.2	1.2	0.57	1.2	14.2
Single-phase voltage drop of 20%	TVC	4.2	1.6	0.8	2.5	17.8
	TDC	3.9	1.5	0.8	2.45	17.8
	MPC+DC	2.5	1.2	0.6	2.6	12.8
	Method proposed	1.3	0.8	0.45	1.5	7.1

During the restoration period of the power grid, the absorbed reactive power is greatly reduced, and the stator flux feedforward compensation accelerates the transient magnetic flux attenuation speed of the stator. GSC provides reactive power support to the grid, further to accelerate the recovery speed of DFIG.

Figure 8 shows operating results under scenario C, the single-phase voltage drops between $t = 1.1$ s and 1.7 s.

During the voltage drop period, the proposed method slowly increases the rotor speed and gradually decreases after the voltage is restored, with a speed overshoot of only 7.1%. The TVC scheme increases the rotor speed by 17.8%. Among the four control strategies, under the TVC and TDC schemes, the rotor current peak values are 4.1 pu and 3.7 pu, which seriously affect the stability of DFIG operation. The method proposed has a significant effect on suppressing rotor overcurrent by injecting reverse current into the rotor through RSC, with a peak rotor current of 1.3 pu. DC bus voltage overshoot by the method is only 0.8%. The reactive power absorbed during the restoration of the grid is 1.5 kW, which is 40% less than that under the TVC scheme. The transient magnetic flux attenuation speed of the stator is accelerated, and the reactive power of the stator is restored to a stable state more quickly.

Table 3 lists the rotor speed, current, and stator active and reactive power indicators of DFIG under three scenarios. During power grid faults, the rotor current of TVC is high, absorbing a large amount of reactive power, which is not conducive to the recovery of grid voltage. The use of TDC can accelerate the decay rate of stator flux, but the effect on suppressing rotor current is limited. The control strategy proposed can not only reduce rotor overcurrent but also accelerate the decay rate of stator magnetic flux, provide reactive power to the grid, reduce stator and rotor winding losses, and accelerate the recovery speed of power grid faults.

6. Conclusion

A transient magnetic flux and reactive power compensation control strategy based on MPC for DFIG is proposed. In the RSC control strategy, reverse rotor current compensation is introduced to suppress rotor overcurrent during LVRT. Reactive power support for grid voltage recovery is provided by combining GSC and RSC reactive power allocation strategies, as well as reducing the total loss of DFIG windings. Compared with traditional vector control strategies, the stator flux feedforward control accelerates the transient flux decay rate of the stator, and LVRT capability of DFIG is improved. Specially, by the proposed control strategy under scenario C, the peak rotor current is reduced by 69%, the overshoot of the DC bus voltage by 50%, and the reactive power absorption of the stator by 40%. In addition, during the LVRT process, the rotor speed overshoot is controlled, which increases the stability of the wind power generation system. Therefore, the control strategy proposed would own a good application in this field.

Nomenclature

DFIG: Doubly fed induction generator
GSC, RSC: Grid side converters and rotor side converters
LVRT: Low-voltage ride through
MPC: Model predictive control
MPC+DC: Model predictive control and demagnetization control
MSTOGI: Mixed second- and third-order generalized integrator
TDC: Traditional demagnetization control
TVC: Traditional vector control
WECS: Wind energy conversion system

Symbols

P_m, C_p: Wind energy capture power, power coefficient
v, λ, β: Wind speed, tip speed ratio, yaw angle
ρ, r, η: Air density, turbine radius, gearbox ratio
ω_t, ω_r: Fan blade angular velocity, DFIG rotor speed
ω_s: Synchronous angular velocity of the power grid
P_s, Q_s, S_s: Active and reactive power on the stator side and stator side capacity
P_r, Q_r, S_r: Active and reactive power on the rotor side and rotor side capacity
Q_{mc}, v_l, f_s: DFIG magnetization reactive power, grid frequency, grid line voltage
I_s, I_r: Effective value of stator and rotor line current
R_s, R_r: Stator and rotor winding resistance
τ: Reactive power distribution coefficient on the GSC and RSC
W_s, W_r, W_{all}: Loss of stator and rotor windings and total loss
$D_1(s)$, $Q_1(s)$: Transfer function expressions of the improved MSTOGI
k, ω_0: Damping coefficient, resonant frequency
ω_1: Frequency of the compensation phase
p, d: Differential operator, voltage drop depth
φ_{sf}, φ_{sn}: Steady-state flux and DC transient flux in stator coordinate system
u_m^+, u_m^-, u_{m0}, τ_s: Amplitude of positive sequence, negative sequence, and zero sequence voltage components, stator time constant
φ_{sf}^+, φ_{sf}^-: Steady-state magnetic flux generated by stator positive and negative sequence voltages
k_s, σ: Stator coupling coefficient, motor leakage coefficient
u_{rk}, u_{rf}, u_{rn}: Open circuit voltage, steady-state flux- and transient flux-induced electromotive force of rotor in stator coordinate system
u_{rk}^r, u_{rf}^r, u_{rn}^r: Open circuit voltage, steady-state flux- and transient flux-induced electromotive force of the rotor in the rotor coordinate system
u_r^r, i_{rn}^r: Rotor voltage and transient current in the rotor coordinate system
c_{sn0}^r, τ_1: Transient DC flux initial value, new stator time constant
λ_s: Characteristic roots of stator flux state equation.

Data Availability

There are no data available.

Conflicts of Interest

The authors declare that there are no conflicts of interest regarding the publication of this paper.

Acknowledgments

This work is part of the Innovative Research Group Project of the National Natural Science Foundation of China (No. 52377104) and the Industry Prospects and Key Core Technologies of Key R&D Programs in Jiangsu Province—competitive project (BE2021063). The authors would like to thank the support from both the Ministry of Science and Technology and National Natural Science Foundation of China. Chinese invention patents are resulting from the work as follows: (1) a software and hardware integrated automatic grid connection switch control system and method for new energy generation (authorization number: ZL201910298681.7, public date: 2020/12/29); (2) a method for adjusting three-phase voltage PLL with improved MSTOGI structure and nonlinear PI control (authorization number: ZL202310185190.8, public date: 2023/11/14); and (3) a LVRT control method for transient flux and reactive power compensation of doubly fed wind turbines based on MPC (application number: CN202311083964.2, application date: 2023/08/28).

References

[1] Z. Zhang, M. Zhou, Z. Wu, S. Liu, Z. Guo, and G. Li, "A frequency security constrained scheduling approach considering wind farm providing frequency support and reserve," *IEEE Transactions on Sustainable Energy*, vol. 13, no. 2, pp. 1086–1100, 2022.

[2] B. Hamid, I. Hussain, S. J. Iqbal, B. Singh, S. Das, and N. Kumar, "Optimal MPPT and BES control for grid-tied DFIG-based wind energy conversion system," *IEEE Transactions on Industry Applications*, vol. 58, no. 6, pp. 7966–7977, 2022.

[3] Z. Guo, W. Wei, M. Shahidehpour, L. Chen, and S. Mei, "Two-timescale dynamic energy and reserve dispatch with wind power and energy storage," *IEEE Transactions on Sustainable Energy*, vol. 14, no. 1, pp. 490–503, 2023.

[4] C. Du, X. Du, and C. Tong, "SSR stable wind speed range quantification for DFIG-based wind power conversion system considering frequency coupling," *IEEE Transactions on Sustainable Energy*, vol. 14, no. 1, pp. 125–139, 2023.

[5] B. Hu, H. Nian, M. Li, and Y. Xu, "Impedance characteristic analysis and reshaping method of DFIG system based on DPC without PLL," *IEEE Transactions on Industrial Electronics*, vol. 68, no. 10, pp. 9767–9777, 2021.

[6] D. Jiang, W. Yu, J. Wang, G. Zhong, and Z. Zhou, "Dynamic analysis of DFIG fault detection and its suppression using sliding mode control," *IEEE Journal of Emerging and Selected Topics in Power Electronics*, vol. 11, no. 1, pp. 643–656, 2023.

[7] Z. Zheng, D. Song, K. Du, X. Xiao, J. Ren, and Q. Xie, "A continuous fault ride-through scheme for DFIGs under commutation failures in LCC-HVDC transmission systems," *Journal of Modern Power Systems and Clean Energy*, vol. 11, no. 4, pp. 1126–1135, 2023.

[8] N. Jabbour, E. Tsioumas, C. Mademlis, and E. Solomin, "A highly effective fault-ride-through strategy for a wind energy conversion system with a doubly fed induction generator," *IEEE Transactions on Power Electronics*, vol. 35, no. 8, pp. 8154–8164, 2020.

[9] K.-J. Du, X.-Y. Xiao, Y. Wang, Z.-X. Zheng, and C.-S. Li, "Enhancing fault ride-through capability of DFIG-based wind turbines using inductive SFCL with coordinated control," *IEEE Transactions on Applied Superconductivity*, vol. 29, no. 2, pp. 1–6, 2019.

[10] R. H. Yang and J. X. Jin, "Unified power quality conditioner with advanced dual control for performance improvement of DFIG-based wind farm," *IEEE Transactions on Sustainable Energy*, vol. 12, no. 1, pp. 116–126, 2021.

[11] L. Zhou, J. Liu, and S. Zhou, "Improved demagnetization control of a doubly-fed induction generator under balanced grid fault," *IEEE Transactions on Power Electronics*, vol. 30, no. 12, pp. 6695–6705, 2015.

[12] S. Xiao, G. Yang, H. Zhou, and H. Geng, "An LVRT control strategy based on flux linkage tracking for DFIG-based WECS," *IEEE Transactions on Industrial Electronics*, vol. 60, no. 7, pp. 2820–2832, 2013.

[13] D. Zhou and F. Blaabjerg, "Optimized Demaginizing Control of DFIG Power Converter for Reduced Thermal Stress During Symmetrical Grid Fault," *IEEE Transactions on Power Electronics*, vol. 33, no. 12, pp. 10326–10340, 2018.

[14] S. Chen, J. Yao, J. Pei et al., "Transient stability analysis and improved control strategy for DC-link voltage of DFIG-based WT during LVRT," *IEEE Transactions on Energy Conversion*, vol. 37, no. 2, pp. 880–891, 2022.

[15] D. Kumar and K. Chatterjee, "Design and analysis of artificial bee-colony-based MPPT algorithm for DFIG-based wind energy conversion systems," *International Journal of Green Energy*, vol. 14, no. 4, pp. 416–429, 2017.

[16] S. S. Sahoo, K. Chatterjee, and P. M. Tripathi, "A coordinated control strategy using supercapacitor energy storage and series dynamic resistor for enhancement of fault ride-through of doubly fed induction generator," *International Journal of Green Energy*, vol. 16, no. 8, pp. 615–626, 2019.

[17] P. Sun, J. Yao, R. Liu, J. Pei, H. Zhang, and Y. Liu, "Virtual capacitance control for improving dynamic stability of the DFIG-based wind turbines during a symmetrical fault in a weak AC grid," *IEEE Transactions on Industrial Electronics*, vol. 68, no. 1, pp. 333–346, 2021.

[18] Z. Din, J. Zhang, Y. Zhu, Z. Xu, and A. El-Naggar, "Impact of grid impedance on LVRT performance of DFIG system with rotor crowbar technology," *IEEE Access*, vol. 7, pp. 127999–128008, 2019.

[19] M. Liu, W. Pan, Y. Rao et al., "An electromagnetic transient analysis model for DFIG considering LVRT hardware protection," *IEEE Access*, vol. 9, pp. 32591–32598, 2021.

[20] G. F. Gontijo, T. C. Tricarico, L. F. da Silva et al., "Modeling, control, and experimental verification of a DFIG with a series-grid-side converter with voltage sag, unbalance, and distortion compensation capabilities," *IEEE Transactions on Industry Applications*, vol. 56, no. 1, pp. 584–600, 2020.

[21] M. M. Islam, K. M. Muttaqi, and D. Sutanto, "A novel saturated amorphous alloy core based fault current limiter for improving the low voltage ride through capability of doubly-fed induction generator based wind turbines," *IEEE Transactions on Industry Applications*, vol. 57, no. 3, pp. 2023–2034, 2021.

[22] D. Vijay, B. Singh, and G. Bhuvaneswari, "Grid-tied battery integrated wind energy generation system with an ability to operate under adverse grid conditions," *IEEE Transactions on Industry Applications*, vol. 56, no. 6, pp. 6882–6891, 2020.

[23] H. Nian, B. Hu, Y. Xu, C. Wu, L. Chen, and F. Blaabjerg, "Analysis and reshaping on impedance characteristic of DFIG system based on symmetrical PLL," *IEEE Transactions on Power Electronics*, vol. 35, no. 11, pp. 11720–11730, 2020.

[24] S. Ghosh, Y. J. Isbeih, R. Bhattarai, M. S. E. Moursi, E. F. El-Saadany, and S. Kamalasadan, "A dynamic coordination control architecture for reactive power capability enhancement of the DFIG-based wind power generation," *IEEE Transactions on Power Systems*, vol. 35, no. 4, pp. 3051–3064, 2020.

[25] Y. Hu, T. K. Chau, X. Zhang, H. H.-C. Iu, T. Fernando, and D. Fan, "A novel adaptive model predictive control strategy for DFIG wind turbine with parameter variations in complex power systems," *IEEE Transactions on Power Systems*, vol. 38, no. 5, pp. 4582–4592, 2023.

[26] R. Errouissi, A. Al-Durra, S. M. Muyeen, S. Leng, and F. Blaabjerg, "Offset-free direct power control of DFIG under continuous-time model predictive control," *IEEE Transactions on Power Electronics*, vol. 32, no. 3, pp. 2265–2277, 2017.

[27] Y. Zhang, S. Zhang, T. Jiang, J. Jiao, and W. Xu, "A modified model-free predictive current control method based on an extended finite control set for DFIGs applied to a nonideal grid," *IEEE Transactions on Industry Applications*, vol. 58, no. 2, pp. 2527–2536, 2022.

[28] P. Kou, D. Liang, J. Li, L. Gao, and Q. Ze, "Finite-control-set model predictive control for DFIG wind turbines," *IEEE Transactions on Automation Science and Engineering*, vol. 15, no. 3, pp. 1004–1013, 2018.

[29] F. E. Z. Magdy, H. M. Hasanien, W. Sabry, Z. Ullah, A. Alkuhayli, and A. H. Yakout, "Mountain gazelle algorithm-based optimal control strategy for improving LVRT capability of grid-tied wind power stations," *IEEE Access*, vol. 11, pp. 129479–129492, 2023.

[30] S. Puchalapalli and B. Singh, "A novel control scheme for wind turbine driven DFIG interfaced to utility grid," *IEEE Transactions on Industry Applications*, vol. 56, no. 3, pp. 2925–2937, 2020.

[31] J. Ren, X. Xiao, Z. Zheng, and Z. Ma, "A SMES-based dynamic current limiter to improve the LVRT capability of DFIG-based WECS5401805," *IEEE Transactions on Applied Superconductivity*, vol. 31, no. 8, pp. 1–5, 2021.

[32] H. Geng, C. Liu, and G. Yang, "LVRT capability of DFIG-based WECS under asymmetrical grid fault condition," *IEEE Transactions on Industrial Electronics*, vol. 60, no. 6, pp. 2495–2509, 2013.

[33] R. Zhu, Z. Chen, X. Wu, and F. Deng, "Virtual damping flux-based LVRT control for DFIG-based wind turbine," *IEEE Transactions on Energy Conversion*, vol. 30, no. 2, pp. 714–725, 2015.

[34] Y. W. Shen, D. P. Ke, W. Qiao, Y. Z. Sun, D. S. Kirschen, and C. Wei, "Transient reconfiguration and coordinated control for power converters to enhance the LVRT of a DFIG wind turbine with an energy storage device," *IEEE Transactions on Energy Conversion*, vol. 30, no. 4, pp. 1679–1690, 2015.

[35] Y. M. Alsmadi, L. Xu, F. Blaabjerg et al., "Detailed investigation and performance improvement of the dynamic behavior of grid-connected DFIG-based wind turbines under LVRT conditions," *IEEE Transactions on Industry Applications*, vol. 54, no. 5, pp. 4795–4812, 2018.